2017 IEEE/RSJ International Conference on Intelligent Robots and Systems (IROS)
September 24–28, 2017, Vancouver, BC, Canada

A Self-Folding Robot Arm for Load-Bearing Operations

Chang Liu[1] and Samuel M. Felton [1]

Abstract— **Self-folding is capable of forming complex three-dimensional structures from planar sheets. However, existing self-folding machines cannot generate large forces or bear high loads. In contrast, traditional robots are expected to operate under large loads but these robots are generally dense, resulting in heavy machines with relatively low strength-to-weight ratios. In this paper, we present a new self-folding technique that is meter-scale and load-bearing. We demonstrate the design and fabrication of both structural beams and pneumatically actuated joints. We model and measure the stiffness and strength of self-folded structural beams. Finally, we integrate these results into a robotic arm that weighs 0.3 kg and can lift up to 1.0 kg. These results indicate that functional, load-bearing, self-folding robots are possible.**

I. Introduction

Origami engineering has many strengths: it enables inexpensive and rapid manufacturing [1], it can produce both small (micrometer) and large (decameter) structures [2], [3], and it is capable of complex geometries [4]. One particular application is the creation of strong, light-weight structures, and this has been used in products from corrugated cardboard to full-size buildings [3], [5].

Within origami engineering, self-folding is a versatile field with many implementations and applications [6]–[8]. It has even been used to build robots [9], [10]. However, existing self-folding devices are small and fragile. Most research on self-folding techniques is done on the micrometer or millimeter scale [11], [12], due to the small torques exerted by the self-actuated hinges. Larger examples are often made from flimsy materials such as paper, and have trouble supporting their own weight at length scales of decimeters [9], [13]. The resulting fragility limits their maximum size, function, and lifespan.

One potential solution is pneumatic self-folding. Pouch motors have been demonstrated as a lightweight and inexpensive actuator for both assembly and actuation [14]. These have been integrated into self-folding structures and machines [15], [16]. However, previous implementations were limited to the centimeter length scale and did not demonstrate the ability to withstand substantial loading.

Another relevant field is fluidic origami, in which an enclosed folded structure is filled with a fluid to induce volumetric expansion [17]. Similar to other soft actuators, the shape of the fluidic origami structure changes with fluid volume. However, the fold pattern confines the structure to a particular motion pattern [17], [18], and the changing geometric pattern can result in large changes to stiffness and strength [5].

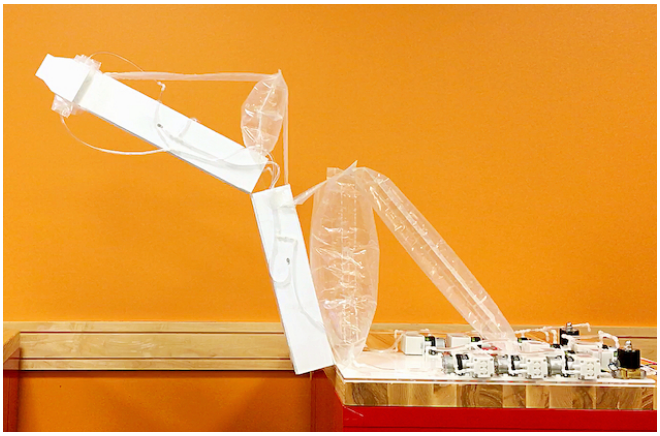

Fig. 1: A self-folding arm driven by pneumatic pouches that weighs 0.3 kg (not including pumps), can lift 1.0 kg objects, and has a reach of 65 cm

In this paper we present a new self-folding paradigm that combines pouch motors with pop-up style fluidic origami to create load-bearing, self-folding machines. We identify, build, and test three fold patterns for structural elements, and a design for load-bearing joints actuated with pouch motors. We derive and validate the mathematical models for the beam stiffness and the joint torque. Finally, we demonstrate the potential of this technique in a 0.3 kg, two degree-of-freedom (DOF) robotic arm that can lift 1.0 kg over a range of 65 cm.

II. Design

Previous work has demonstrated that self-folding machines are capable of arbitrary motions if they can produce linkage assemblies [13]. In this paper, we consider two general categories of machine components: structural linkages and actuated joints. These two elements can be combined to produce linkage assemblies, satisfying the design requirement for complex kinematics. To demonstrate this, we designed 2-DOF robotic arm.

A. Linkage Design

The linkage design consists of three parts: the laminate design, consisting of the materials and order in which they're layered; the fold pattern, which dictates where the hinges are embedded in the laminate and how far they fold; and the pouches that actuate the folding.

[1] College of Engineering, Northeastern University, Boston, MA 02115, USA liu.chang7@husky.neu.edu s.felton@northeastern.edu

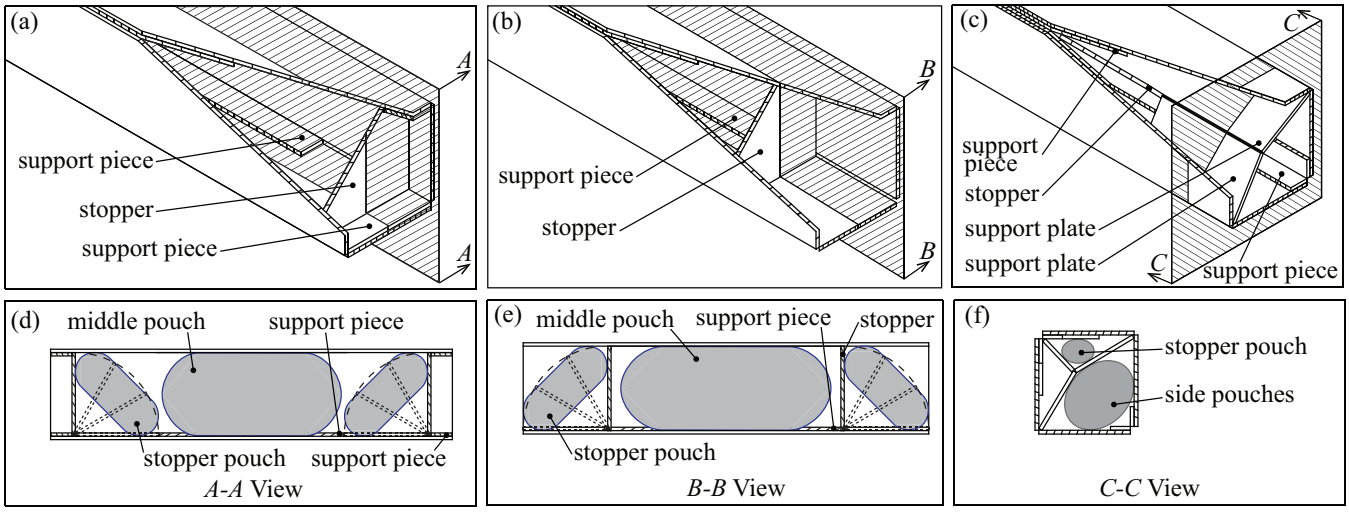

Fig. 2: Isometric and cross-sectional drawings of the three fold patterns tested in this paper. (a,d) Design 1. (b,e) Design 2. (c,f) Design 3.

1) Laminate Design: We use a laminate design that is similar to those used in previous devices [19], [20]. The laminate design consists of a structural layer (a corrugated plastic sheet), and a flexural layer (an adhesive-backed polyester film). The flexural layer provides flexibility at the self-folding hinges, while the structural layers maintain rigidity elsewhere. The pairing of a single structural layer and a single flexural layer forms a sublaminate that can be fabricated to include flexural hinges. These sublaminates are then combined into multi-layer laminates to enable pop-up style folding.

2) Fold Pattern Design: In this paper we present three fold patterns, each of which was tested in the form of a cuboid beam 86 mm tall, 86 mm wide, and 381 mm long. Design 1 and Design 2 use stoppers to hold the square shape of the beam. Design 3 uses a bistable feature oriented diagonally in the beam cross-section to test the efficacy of a bistable feature that is uniform along the length of the beam.

Design 1 (Fig. 2a) includes three sublaminate layers. Two stoppers are placed at both ends of the beam, and two support pieces are placed at each end of the beam (Fig. 2d) to prevent the stoppers from rotating over 90°. For actuation, one big pouch is placed inside the beam to push up the walls, and two small pouches are placed at the stoppers to push them up (Fig. 2d). The weight of each sample is 0.13 kg on average.

Design 2 (Fig. 2b) includes three sublaminate layers. This design is similar to Design 1, except for two differences: 1) the stoppers are pushed up in opposite directions; 2) the support pieces are located further inward (Fig. 2e). The weight of each sample is 0.13 kg on average.

Design 3 (Fig. 2c) includes four sublaminate layers. In this design, diagonal support plates are used to push up the beam and lock the structure to rectangle shape. A stopper is used to prevent the support plates from folding further, holding them at the diagonal. For actuation, two pouches are placed at both ends inside the support plates to push up the walls and push up the support plates at the same time. One small long pouch is placed at the stopper to drive the stopper's movement. The weight of each sample is 0.18 kg on average.

3) Pouch Design: The pouch motors used in this paper are similar to those presented by Niiyama et al. [14]. The pouches are made using 100 µm low-density polyethylene (LDPE) film and sealed using line impulse sealer. A small opening is left at one side to insert the tubing that connects the pouch to the pumps. After the tubing is inserted, we use hot-melt adhesive to seal the small opening. Pouches used to actuate the joints are reinforced with tape to increase their maximum pressure.

Pouches are placed in the beam to actuate the self-folding procedure, and placed at the joints of the arm to actuate the lifting capability. The placement of the pouches in the beam are based on their function and the fold pattern geometry (Fig. 2d-f). Details about the joint pouches are in Section II-B.2.

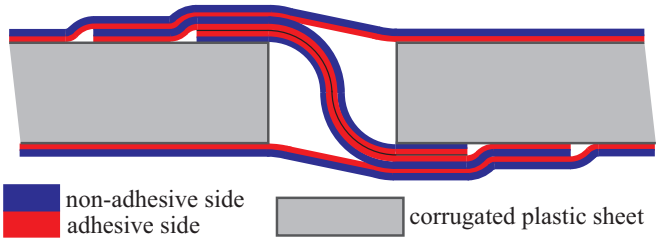

Fig. 3: The joints in each sublaminate are flexural hinges designed to increase structural integrity. Each joint includes one adhesive layer on either side of the sublaminate and two layers in the middle that attach to opposing sides of the adjacent structural layers.

B. Joint Design

Joints are built to connect two rigid beams with a single rotational degree of freedom. They must be sufficiently stiff to resist rotation in off-axis directions and resist delamination. Each actuated joint consists of a flexural hinge and a pouch motor assembly, consisting of a pouch and inextensible tendons.

1) Flexural Hinge: Two sublaminates from each of the beams are connected by a hinge (Fig. 3). Two layers of adhesive-backed polyester film are pasted face-to-face on the adhesive side at the end of the film, and the rest adhesive parts are pasted to two beam walls. Then another two layers are pasted on the outside to align the two beam walls. By using this design, the two beams can rotate freely along its primary axis while resisting shear forces and off-axis rotations.

2) Pouch Actuation Design: One pouch is placed at the elbow joint and two pouches are placed at the shoulder joint (Fig. 4). The wider pouch at the shoulder joint is used for lifting the beam during operation and the thinner one is used to push the beam up during assembly. These pouches are attached to inextensible tendons that are connected to the far ends of the linkages. As the pouches are being inflated those pouches will push the tendons. The tendons will then exert forces on the end of the beams on either side of the joint, creating a torque on the joint.

C. Robotic Arm Design

To demonstrate usage of the beam design, we make a 2-DOF robotic arm consisting of two structural linkages of length $L = 38\,\text{cm}$, width $L_w = 8.6\,\text{cm}$, and two joints – the shoulder joint connecting the lower linkage to the base, and the elbow joint connecting the lower and upper linkages (Fig. 4). A gripper is attached to the arm at the end of the upper linkage.

1) Pneumatic Actuation: To actuate the pouches, we use 10 pneumatic pumps (U.S. Solid, RSV00008) to provide the necessary flow rates. Six pumps are used on the shoulder pouches: three to inflate the pouch, and three to vacate it. Two pumps are used on the elbow pouch: one for inflation, and one for vacating. One pump is used to actuate the beam pouches during assembly and one pump is used to control the gripper. Two solenoid valves (Senya, 2w-025-08) are used in combination with the two sets of vacating pumps in order to close and open the release valves.

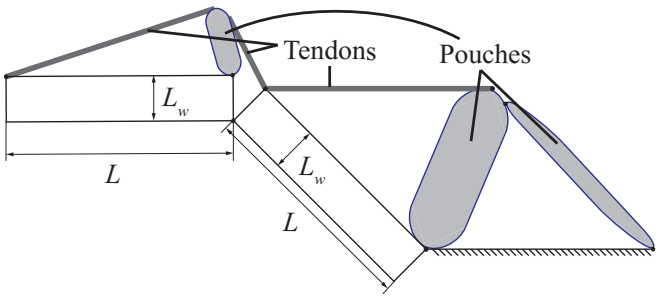

Fig. 4: The elbow and shoulder joints are actuated by pouch motors and tendons.

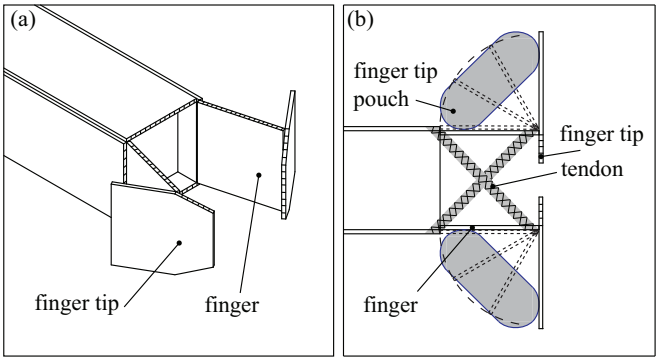

Fig. 5: (a) The gripper design with four degrees of freedom including articulated two-segment fingers. (b) The finger is actuated by two pouches with antagonistic force supplied by two tendons.

2) Gripper Design: A 2-DOF gripper is attached to the end of the robotic arm. A cross-tendon design is used to support and hold the grasped object, and finger pouches are used to actuate the fingertips.

III. Fabrication

Corrugated plastic sheets (0.125" thick) are cut using a CO_2 laser cutter into panels that make up the laminate (Fig. 6a). These layers are combined to create the beam walls (Fig. 6b). The support pieces are pasted to the beam walls using double sided adhesive transfer tape (ATT). Polyester adhesive-backed film (PABF) is used to connect the walls. The stoppers are then connected to the corners with PABF (Fig. 6c). Pouches are placed based on their functions – the stopper pouches are placed under the stoppers to push them up, and the middle pouch is placed inside the beam to actuate the beam from flat to standing (Fig. 6d). Initially the middle pouch is set flat, and the stopper pouches are compressed beneath the stoppers as the stoppers fold back (Fig. 6e). Four of the beam walls are assembled edge-to-edge with PABF (Fig. 6f), folded over, and the distal edges are sealed to create closed loop that lays flat (Fig. 6g). This structure can then be inflated to form the final beam shape (Fig. 6h). Pop-up beam structure is shown in Figure 6h.

IV. Modeling

A. Beam Structure Modeling

1) Bending: The deflection of the folded beams occurs in three phases, resulting in three distinct stiffness regimes. First, when the deflection is smaller than the thickness of the beam wall t, the probe of the multitester contacts the top face which is only loosely connected with the side walls. Therefore, the stiffness of the beam is only due to the bending of the top face, resulting in a force F_t. Second, as the deflection reaches the top of the side walls, they also bear some portion of the load, resulting in an additional reaction force F_b. Third, when the force in the side walls reaches the

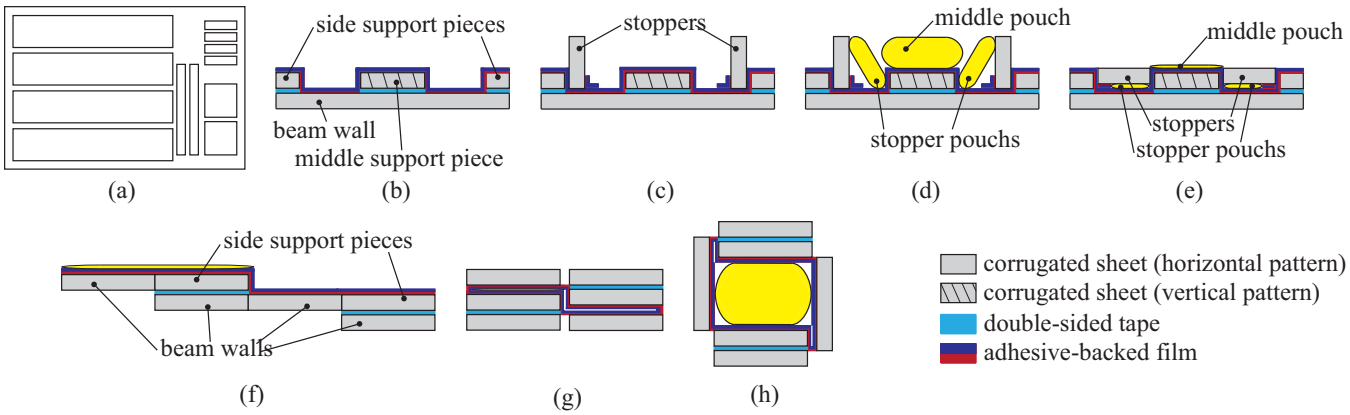

Fig. 6: Fabrication steps for Design 1. (a) The structural panels are cut from a single sheet of corrugated plastic. (b) Each beam wall is assembled by hand (lengthwise view). (c) Stoppers are installed (lengthwise view). (d) Pouches are installed (lengthwise view). (e) Stoppers are folded down (lengthwise view). (f) Four beam walls are joined (axial view). (g) The beam is folded over and collapsed (axial view). (h) When inflated, the beam forms its desired shape (axial view).

buckling load $F_{cr} = F_{b,max}$, the stiffness enters a new regime. Due to the anisotropic structure in the structural panels, this regime is difficult to model so we assume that the force due to the sidewalls remains constant.

These three regimes can be combined into a single equation for the bending force F shown in equation 1.

$$F = \begin{cases} F_t & \delta < t \\ F_t + 2F_b & \delta \geq t,\ F_b < F_{cr} \\ F_t + 2F_{cr} & F_b \geq F_{cr} \end{cases} \tag{1}$$

For the bending forces on the top surface and the side walls, we use equation 3 [21] and the corresponding moment of inertia can be expressed in equation 2 [21], with the corresponding dimensions.

$$I = \frac{bh^3}{12} \tag{2}$$

$$F_{bend} = \frac{48EI\delta}{L^3} \tag{3}$$

$$F_t = \frac{4EL_w t^3 \delta}{L^3} \tag{4}$$

$$F_b = \frac{4EtL_w^3 \delta}{L^3} \tag{5}$$

b is the width of the beam, h is the height of the beam, L is the length of the beam between the supports, L_w is the width and thickness of the beam, and E is the modulus of elasticity.

Buckling occurs when the force reaches the critical buckling load, which is defined in equation 6 [22].

$$F_{cr} = \frac{\pi^2 EI}{l^2} \tag{6}$$

2) One-inch compression: For the one-inch compression test we observe the same three regimes. In the first regime, the top face bends, resulting in a force F_t. Second, the side walls compress, generating a force F_c. Third, the side walls buckle at a force F_{cr}, (calculated using equation 6), and the load due to the side walls is assumed to be constant from that point on. These three regimes can be combined into a single equation representing the compressive force F (equation 7).

$$F = \begin{cases} F_t & \delta < t \\ F_t + 2F_c & \delta \geq t, F_c < F_{cr} \\ F_t + 2F_{cr} & F_c \geq F_{cr} \end{cases} \tag{7}$$

The beam's compression force can be modeled using equation 8 [22].

$$F_c = \frac{EA}{l}\delta \tag{8}$$

where δ is the deflection of the beam, l is the width of the beam wall, E is the Young's Modulus, F_c is the force exerting in the beam wall, A is the cross sectional area of the beam wall that exerting force.

3) Six-inch compression: For the six-inch compression test, there are also three regimes. The only difference is that the stopper in designs 2 and 3 is also supporting a portion of the load F_{cs}, and due to their position underneath the top face they are under compression during all three regimes.

$$F = \begin{cases} F_t + F_{cs} & \delta < t \\ F_t + F_{cs} + 2F_c & \delta \geq t, F_c < F_{cr} \\ F_t + F_{cs} + 2F_{cr} & F_c \geq F_{cr} \end{cases} \tag{9}$$

B. Arm Modeling

The joints are actuated by a central pouch motor attached at one end to the flexural hinge, and at the other to two tendons that connect to the far end of either linkage (Fig. 4). In the shoulder joint design, one of the tendons is also a pouch, but that pouch does not contribute noticeably to the actuation of the arm. Instead, it is used during the self-folding

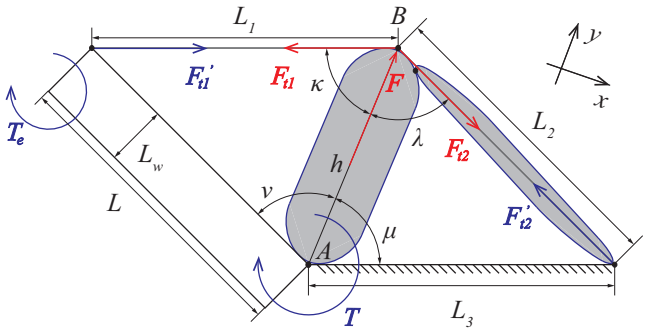

Fig. 7: Idealized geometry and forces of the pouch actuation model.

process to push the lower linkage upright (see Supplemental Video).

1) Pouch Modeling: The pouches used in the arm are all considered as cylinders in this model. Each pouch is initially deflated with a negligible height and an area A. As each pouch is inflated, the maximum longitudinal force F exerted by the pouch is equal to AP, where P is the internal pressure. This assumes that the tension in the pouch walls is negligible, which is reasonable when the pouch is not at its maximum length.

2) Pouch Motor Modeling: A generalized model of pouch actuation is shown in Figure 7. The relationships between the angles and the length of the beam and tendons can be found in equations 10 through 13.

$$\cos\kappa = \frac{L^2 - L_1^2 - h^2}{2L_1 h} \tag{10}$$

$$\cos\lambda = \frac{L_3^2 - L_2^2 - h^2}{2L_2 h} \tag{11}$$

$$\cos\nu = \frac{L_1^2 - L^2 - h^2}{2Lh} \tag{12}$$

$$\cos\mu = \frac{L_2^2 - L_3^2 - h^2}{2L_3 h} \tag{13}$$

L is the length of the beam, h is the height of the should pouch, L_1 and L_2 are the length of the tendons, and L_3 is the distance from the shoulder to the base tendon connection point. κ, λ, ν, μ are all functions of the inner pressure of the shoulder pouch and the L_i.

We obtain the tension forces in the tendons from equations 14 and 15.

$$\sum F_x = 0 \quad -F_{t1}\sin\kappa + F_{t2}\sin\lambda = 0 \tag{14}$$

$$\sum F_y = 0 \quad F - F_{t1}\cos\kappa - F_{t2}\cos\lambda = 0 \tag{15}$$

F_{t1} and F_{t2} are the tension force in the tendons, and F is the force exerting by the pouch.

The torque T at the joint can be solved with equation 16.

$$T = F_{t1} L \sin(\pi - \kappa - \nu) + T_e \tag{16}$$

Therefore, given a joint with fixed tendon lengths and attachment points, the joint torque is dependent on the pouch pressure and the joint angle.

V. Experiments and Results

We performed three structural tests – a three-point bending test, a one-inch compression test at one end, and a six-inch compression test at one end (Fig. 8) – on the three folded linkage designs. Each test was performed on 10 samples with a Mecmesin Multi-Test 2.5i (250 N load cell). Note that in certain conditions the load cell reached its limit before full displacement was reached, so some results are truncated.

A. Three Point Bending Test

The three-point bending test was applied to each beam design to test the bending stiffness of the beams (Fig. 8a,d,g). The results indicate that Designs 1 and 2 are substantially stiffer than Design 3 for displacements between 0 and 20 mm. However, Design 2 shows a decrease in reactive force after this point, likely related to buckling of the sidewalls.

The model underestimates the results for all three designs in the first regime, where only the top surface is interacting. The main reason is that the model assumes the side faces and top face are not connected, but the PABF does provide some structural coupling so that the sidewalls do contribute to the beam stiffness in the first regime. During the second section, the model overestimates the performance. The main reason is due to the pattern of the corrugated plastic sheet. As the probe is pushing down, the contacting point on the corrugated sheet starts to crack. Design 3 underperforms Designs 1 and 2 because the diagonal stopper does not adequately maintain the square cross-section, allowing the side faces to tilt into a parallelogram cross-section.

B. One-Inch Compression Test

The one-inch compression test was applied to each beam design to measure orthogonal stiffness to the beam's end. This test was particularly important because it mimics the force that a beam may feel when supporting a hinge that is under an orthogonal load, such as when lifting an object. Results show that Design 1 is the stiffest. This was expected due to the distal placement of the stoppers, which provide additional structural support at their location.

The model matches the result from Design 1, but overestimated Design 2 and Design 3. For Design 2, the stopper is away from the contact area, which case nothing to hold the top surface on one side. For Design 3, the diagonal stopper fails to maintain a square cross-section.

C. Six-Inch Compression Test

The six-inch compression test was applied to each beam design to measure orthogonal stiffness to the beam along its length. In this case, Design 2 slightly outperformed Design 1. This is likely due to the more central placement of the stopper relative to the center of pressure. In both cases, the model overestimates the stiffness, which we believe is because in both cases the stoppers are not at the center of pressure. Design 3, like in previous experiments, failed to maintain a square cross-section, resulting in the physical specimens underperforming the model.

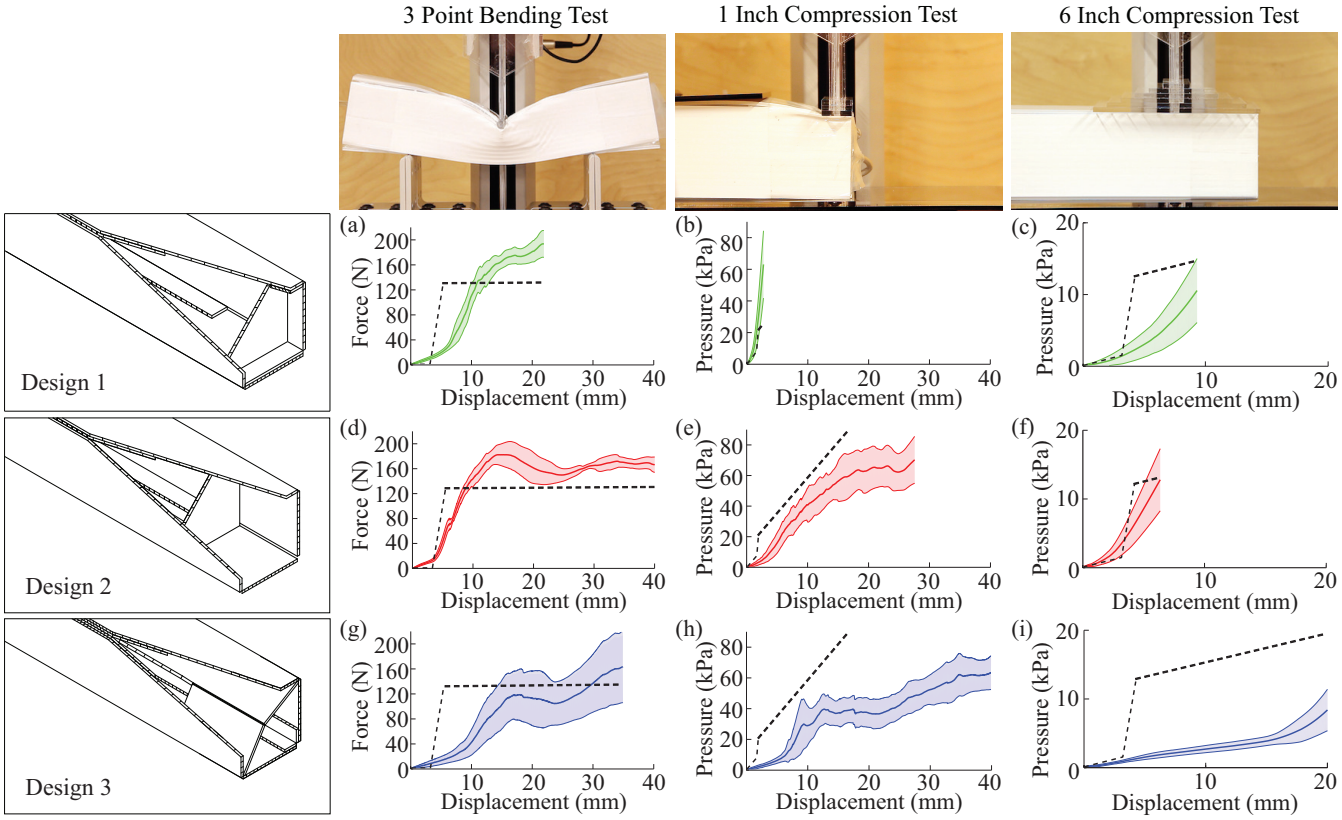

Fig. 8: Experimental results of three fold patterns under three different mechanical tests (solid line, shaded region indicates standard deviation, N=10). These are plotted with the analytical predictions (dashed line).

D. Torque

In order to validate the pouch torque model, an actuated joint was fixed at different joint angles (θ of 90°, 120°, 150°, and 180°). The pressure in the pouch was varied from 0 to 80 kPa and the torque was measured. The results (Fig. 9) indicate that the model effectively estimates the torque that is exerted.

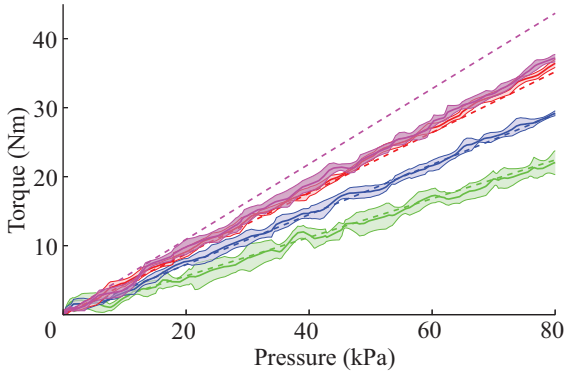

Fig. 9: Experimental (solid line) and modeled (dashed line) torque as a function of pouch pressure at different joint angles. Green: 90°, Blue: 120°, Red: 150°, Megenta: 180°. Shaded region indicates standard deviation, N=5.

E. Self-Folding Arm and Gripper

A robotic arm was fabricated that self-folded and then performed a grasping motion of a distal object (see Supplemental Video). The arm was initially deflated to three layer planar structure with a total height of 4 cm. A dumbbell of 1.0 kg was placed 65 cm away from the arm (Fig. 10a). First, the beam was inflated into its operational form (Fig. 10b). This process took 20 s and the associated pouches were driven at a maximum pressure of 28 kPa and a maximum flow rate of 145 cm^3/s. Second, the pouch motor at the shoulder inflated to push the arm up from 0° to 90° (Fig. 10c). Once in this position, the shoulder joint has an actuated range of 0° to 90°, while the elbow has a range of 0° to 180° (Fig. 10d). The arm reached out and the gripper grabbed the dumbbell through inflation of the gripper pouches (Fig. 10e). Finally, the arm lifted the dumbbell (Fig. 10f). Performance of the complete grasping-and-lifting task took 240 s. The operational pouches (elbow, shoulder, and gripper) were driven at a maximum pressure of 55 kPa.

VI. Discussion

The results indicate that self-folding and load-bearing machines are possible, and the linkage assemblies are capable of bearing the operational forces involved with moving a one-kilogram object. The experimental data indicates that our models are accurately predicting their mechanical behavior, at least under small deformations. In addition, the structural

Fig. 10: The arm (a) in its flat configuration, (b) self-folding, (c) upright, (d) reaching out, (e) grasping, (f) lifting. (g) The elbow pouch. The gripper (h) in position and (i) grabbing a dumbbell.

elements have comparable stiffness to monolithic beams of the same weight made from conventional materials. Consider that a hollow, square aluminum beam with the same weight and a 2 mm wall thickness would have a cross-sectional width of 3.1 cm, and a flexural rigidity $EI = 1.2\,\mathrm{kNm}^2$. The modeled flexural rigidity of Design 1 is approximately $2.4\,\mathrm{kNm}^2$.

The performance of the robotic arm in particular suggests that fluidic origami could create robotic manipulators with superior strength-to-weight ratios compared to existing industrial machines. The total weight of the system is 3.9 kg, demonstrating an effective strength-to-weight ratio of 26%. Moreover, the majority of that weight is made up of the pumps and solenoids. The structure of the robotic arm and actuating pouches only weigh 0.3 kg, which would correlate to a strength-to-weight ratio of 330% if off-board pressurized air were available. A comparison between our robotic arm with existing commercial arms can be found in Table I.

These results also indicate many ways we can improve this technique. One notable weakness is the current implementation of the pouch motor. The examples shown here are very slow, resulting in robotic joints moving at a rate of $4\,^\circ\,\mathrm{s}^{-1}$ on average. They are also bulky and susceptible to off-axis forces pushing them out of alignment. The pumps and valves that drive the pouches account for 92% of the weight of the arm demonstrated here, a reduction in the volume and pressure required to actuate these pouches would substantially reduce the machine's overall weight.

Arm	Mass (kg)	Payload (kg)	Ratio
Lynxmotion AL5A [23]	0.6	0.11	0.18
KUKA KR 3 R540 [24]	26	3	0.11
KUKA KR 6 R700 fivve [25]	48	6	0.13
KUKA KR 20-3 [26]	254	20	0.08
Self-folding arm	**0.3**	**1**	**3.33**
Self-folding with pumps	**3.9**	**1**	**0.26**

TABLE I: Robotic Arm Weight-to-Payload Ratios

The joints themselves are another weak point. Despite our effort to increase their strength and stiffness, delamination continued to be a substantial failure mode and the arm cannot resist significant transverse forces. Further research will investigate new laminate patterns to increase stiffness, and different origami patterns that can result in parallel joints that distribute the load.

Finally, we must investigate how to increase the complexity of the structures and linkage assemblies. All structures demonstrated here were cuboids, which simplified both the fold patterns and the fabrication. Further investigation is necessary to see how challenges such as locking mechanisms and pouch placement will be affected by more complex shapes. The linkage assembly was also limited to a two-dimensional plane, and expanding to three dimensions will introduce new challenges.

References

[1] C. D. Onal, M. T. Tolley, R. J. Wood, and D. Rus, "Origami-inspired printed robots," *IEEE/ASME Transactions on Mechatronics*, vol. 20,

no. 5, pp. 2214–2221, 2015.

[2] J. Rogers, Y. Huang, O. G. Schmidt, and D. H. Gracias, "Origami mems and nems," *Mrs Bulletin*, vol. 41, no. 02, pp. 123–129, 2016.

[3] W. Gilewski, J. Pelczynski, and P. Stawarz, "Origami inspired timber structures-construction and numerical modelling," *Annals of Warsaw University of Life Sciences-SGGW. Forestry and Wood Technology*, vol. 85, 2014.

[4] T. Tachi, "Origamizing polyhedral surfaces," *IEEE transactions on visualization and computer graphics*, vol. 16, no. 2, pp. 298–311, 2010.

[5] S. Li and K. Wang, "Fluidic origami: a plant-inspired adaptive structure with shape morphing and stiffness tuning," *Smart Materials and Structures*, vol. 24, no. 10, p. 105031, 2015.

[6] G. M. Whitesides and B. Grzybowski, "Self-assembly at all scales," *Science*, vol. 295, no. 5564, pp. 2418–2421, 2002.

[7] N. Bassik, G. M. Stern, and D. H. Gracias, "Microassembly based on hands free origami with bidirectional curvature," *Applied physics letters*, vol. 95, no. 9, p. 091901, 2009.

[8] E. Hawkes, B. An, N. Benbernou, H. Tanaka, S. Kim, E. Demaine, D. Rus, and R. Wood, "Programmable matter by folding," *Proceedings of the National Academy of Sciences*, vol. 107, no. 28, pp. 12 441–12 445, 2010.

[9] S. M. Felton, M. T. Tolley, C. D. Onal, D. Rus, and R. J. Wood, "Robot self-assembly by folding: A printed inchworm robot," in *Robotics and Automation (ICRA), 2013 IEEE International Conference on*. IEEE, 2013, pp. 277–282.

[10] M. E. Nisser, S. M. Felton, M. T. Tolley, M. Rubenstein, and R. J. Wood, "Feedback-controlled self-folding of autonomous robot collectives," in *Intelligent Robots and Systems (IROS), 2016 IEEE/RSJ International Conference on*. IEEE, 2016, pp. 1254–1261.

[11] J.-H. Na, A. A. Evans, J. Bae, M. C. Chiappelli, C. D. Santangelo, R. J. Lang, T. C. Hull, and R. C. Hayward, "Programming reversibly self-folding origami with micropatterned photo-crosslinkable polymer trilayers," *Advanced Materials*, vol. 27, no. 1, pp. 79–85, 2015.

[12] S. Felton, K. Becker, D. Aukes, and R. Wood, "Self-folding with shape memory composites at the millimeter scale," *Journal of Micromechanics and Microengineering*, vol. 25, no. 8, p. 085004, 2015.

[13] S. Felton, M. Tolley, E. Demaine, D. Rus, and R. Wood, "A method for building self-folding machines," *Science*, vol. 345, no. 6197, pp. 644–646, 2014.

[14] R. Niiyama, X. Sun, C. Sung, B. An, D. Rus, and S. Kim, "Pouch motors: Printable soft actuators integrated with computational design," *Soft Robotics*, vol. 2, no. 2, pp. 59–70, 2015.

[15] X. Sun, S. M. Felton, R. Niiyama, R. J. Wood, and S. Kim, "Self-folding and self-actuating robots: A pneumatic approach," in *Robotics and Automation (ICRA), 2015 IEEE International Conference on*. IEEE, 2015, pp. 3160–3165.

[16] X. Sun, S. M. Felton, R. J. Wood, and S. Kim, "Printing angle sensors for foldable robots," in *Intelligent Robots and Systems (IROS), 2015 IEEE/RSJ International Conference on*. IEEE, 2015, pp. 1725–1731.

[17] D. Kim and R. B. Gillespie, "Origami structured compliant actuator (osca)," in *Rehabilitation Robotics (ICORR), 2015 IEEE International Conference on*. IEEE, 2015, pp. 259–264.

[18] L. Paez, G. Agarwal, and J. Paik, "Design and analysis of a soft pneumatic actuator with origami shell reinforcement," *Soft Robotics*, vol. 3, no. 3, pp. 109–119, 2016.

[19] R. Wood, S. Avadhanula, R. Sahai, E. Steltz, and R. Fearing, "Micro-robot design using fiber reinforced composites," *Journal of Mechanical Design*, vol. 130, no. 5, p. 052304, 2008.

[20] S. M. Felton, M. T. Tolley, B. Shin, C. D. Onal, E. D. Demaine, D. Rus, and R. J. Wood, "Self-folding with shape memory composites," *Soft Matter*, vol. 9, no. 32, pp. 7688–7694, 2013.

[21] B. J. Goodno and J. M. Gere, *Mechanics of Materials*. Cengage Learning, 2016.

[22] J. E. Shigley, *Shigley's mechanical engineering design*. Tata McGraw-Hill Education, 2011.

[23] Lynxmotion. Lynxmotion - AL5A. Accessed 18 July 2017. [Online]. Available: http://www.lynxmotion.com/c-124-al5a.aspx

[24] RobotWorx. KR3 R540. Accessed 18 July 2017. [Online]. Available: https://www.robots.com/kuka/kr3-r540

[25] ——. KR 6 R700 fivve. Accessed 18 July 2017. [Online]. Available: https://www.robots.com/kuka/kr-6-r700-fivve

[26] ——. KR 20-3. Accessed 18 July 2017. [Online]. Available: https://www.robots.com/kuka/kr-20-3